Effect of grain size and temperature on deformation mechanism of commercially pure titanium

Cai CHEN[1], Dong-sheng HAN[1], Yu-tao SONG[2], Ming-chuan WANG[1],
Yu-sheng LI[2], Shun XU[3], Sen YANG[4], Ji-zi LIU[2,5]

1. Sino-French Engineer School, Nanjing University of Science and Technology, Nanjing 210094, China;
2. Nano and Heterogeneous Structural Materials Center, School of Materials Science and Engineering,
Nanjing University of Science and Technology, Nanjing 210094, China;
3. National Key Laboratory of Science and Technology on Materials under Shock and Impact,
School of Materials Science and Engineering, Beijing Institute of Technology, Beijing 100081, China;
4. School of Materials Science and Engineering, Nanjing University of Science and Technology,
Nanjing 210094, China;
5. Center of Analytical Facilities, Nanjing University of Science and Technology, Nanjing 210094, China

Abstract: To investigate the effects of grain size and processing temperature on the deformation behaviors of commercially pure titanium (CP-Ti), the tensile tests were conducted at room temperature (RT) and liquid nitrogen temperature (LNT) on the samples with the average grain size of 2, 9, 23, and 51 μm, respectively. The experimental results based on EBSD and TEM characterizations showed that dislocation slip was the main deformation mechanism at RT, while abundant deformation twins including $\{10\bar{1}2\}$ extension twins, $\{11\bar{2}2\}$ compression twins and some $\{11\bar{2}2\}-\{10\bar{1}2\}$ secondary twins were observed under LNT condition. The transition of deformation modes from dislocation slip to dynamic twinning contributes to the outstanding mechanical properties of the samples with a larger grain size at LNT. Additionally, a modified Hall−Petch relationship was proposed to study the quantitative contribution of average grain size and deformation twins on yield stresses of CP-Ti under LNT condition.
Key words: commercially pure titanium; cryogenic tensile testing; deformation twinning; grain size; crystallographic texture

1 Introduction

Titanium (Ti) and its alloys have a significant prospect of application in various industries owing to their low density, high strength, and ductility, good corrosion resistance and excellent biocompatibility, especially in the fields of aerospace, marine, and biomedicine [1−3]. Besides, Ti alloys have a low thermal expansion coefficient at a cryogenic temperature which is considered to be the ideal structural materials at cryogenic temperature (<77 K) [4,5]. Over the last decades, the deformation mechanism of Ti alloys at ambient temperature has been widely studied [6−9]. As the basic plastic deformation mechanisms, the dislocation slips including basal, prismatic, pyramidal $\langle a \rangle$, and $\langle c+a \rangle$ slip systems are fully understood by numerous researchers [10−12]. Simultaneously, deformation twinning plays an important role in the strain accommodation in hexagonal close-packed (HCP) alloys where the

$\{10\bar{1}2\}\langle10\bar{1}1\rangle$, and $\{11\bar{2}1\}\langle11\bar{2}6\rangle$ extension twins (ETs), $\{11\bar{2}2\}\langle11\bar{2}3\rangle$ and $\{11\bar{2}4\}\langle22\bar{4}3\rangle$ contraction twins (CTs) are frequently observed in the Ti alloys [13−16]. Twinning-induced grain refinement can improve the mechanical properties of the materials [17,18]. However, critical resolved shear stress (CRSS) of slip is thermal-sensitive [19,20]. It has been reported that the CRSS of slip will significantly increase when the deformation temperature is low [5,21]. Thus, the deformation mechanism is surely different from ambient to cryogenic temperature in Ti alloy. Recently, researchers have been focusing on the cryogenic deformation of commercially pure Ti (CP-Ti), which can trigger the activation of abundant deformation twinning. Therefore, the strength and ductility of related Ti alloy could be dramatically improved [22−24]. LEE et al [25] investigated the microstructure evolution of pure Ti sheet at cryogenic temperature through the tensile test. The results reveal that a high area fraction of twinning of 28.3% was mainly contributed by $\{10\bar{1}2\}$ ETs and $\{11\bar{2}2\}$ CTs, and the fracture elongation of sample parallel to rolling direction (RD) increased from 32% to 50% as the deformation temperature changed from 298 to 100 K. However, the grain size effect was not considered.

Generally, the activation of deformation twins is strongly related to the initial texture, strain rate, deformation temperature, and grain size in Ti alloys [26−28]. α-Ti has strong grain-scale size effects due to higher value of CRSS for the easiest dislocation slip in comparison with the other HCP structured alloy [29]. Therefore, twin activation, twin growth, and twin−twin interaction prefer to form in specimens with large grain sizes at room temperature (RT) [28]. However, it will break down the balance competition between dislocation slip and deformation twinning by increasing their CRSS values with decreasing deformation temperature. The deformation twinning will be the dominant mode since the increased magnitude for slip is far higher than that for twinning. HUANG et al [20] studied the effect of the grain size and temperature on the twinning activation and strength−ductility of CP-Ti. They found that at liquid nitrogen temperature (LNT), the transition from grain boundary strengthening to dynamic twinning strengthening resulted in an excellent strength−ductility combination. However, the multiple effects

of dislocation slip and twinning on strengthening under uniaxial loading at cryogenic temperature have not yet been fully understood [5,20,25]. The limited grain size of the deformation mechanism transition from slip to twinning in CP-Ti at cryogenic temperature is also worth studying, which may have a great effect on mechanical properties. Particularly, the traditional Hall−Petch relationship may not well adapt to the deformation at cryogenic temperature due to different deformation mechanisms [6]. Therefore, it is worthwhile to study the cryogenic mechanical properties of CP-Ti in different grain sizes.

In the present work, the mechanical properties and twinning behavior of CP-Ti with different grain sizes at RT and LNT were investigated. Scanning electron backscatter diffraction (EBSD) and transmission electron microscopy (TEM) techniques were used to characterize the microstructure evolution and dislocation motion. The plastic work hardening behavior, twinning-induced grain fragmentation, texture transformation, and plasticity under tension at LNT were discussed. Moreover, the limited grain size for twinning activation was forecast through a modified Hall−Petch relationship, which was proposed to study the quantitative contribution of average grain size and deformation twins on yield stresses of CP-Ti at LNT. The result is useful to control and design the microstructure of hexagonal metals to promote their application under extreme conditions.

2 Experimental

The CP-Ti with the impurities of 0.19% Al, 0.13% V, 0.15% Fe, 0.10% Zr and 0.03% Cr (wt.%) was used in this work. The as-received sheet specimen was firstly annealed at 750 °C for 120 min, and then rolled at RT with a rolling speed of 300 mm/s. The thickness of the specimen was finally reduced by 80% by multi-pass rolling. In order to obtain fully recrystallized samples with different grain sizes, the rolled sample was subsequently annealed at 550 °C for 30 min, 650 °C for 30 min, 750 °C for 30 min, and 750 °C for 60 min, respectively. Flat dog-bone-shaped tension samples were machined from the processed sheets using electrical discharge machining. The gauge dimensions of tensile samples were 15 mm in length, 4 mm in width and 3 mm in thickness. Note

that the length of the samples was parallel to the RD. All tensile specimens were mechanically polished before the test to remove the wire electrode cutting marks. The uniaxial tensile tests were performed on an electronic universal testing machine (Walter-Bai AG LFM−20) along the RD until failure at RT and LNT, with the initial strain rate of 1×10^{-3} s^{-1}. The microstructure of annealed samples with various grain sizes and fractured samples were characterized by optical microscopy (OM, ZEISS Axio Vert A1), scanning electron microscope (SEM, Zeiss Auriga) together with electro backscatter diffraction (EBSD, Oxford Instrument) technique, and transmission electron microscopy (TEM, JEM−F200) on the surface corresponding to the RD and normal direction (ND) plane. The EBSD measurement was performed with the accelerated voltage and scanning step size of 15 kV and 0.3 μm. The specimen surfaces were prepared by mechanical grinding and further electropolished by using a solution of 10% perchloric acid and 90% acetic acid at 45 V for 50 s at RT until the mirror surface met the surface quality requirements. The TEM samples were thinned with an electrolytic double jet thinning instrument for 80−100 s, under a working current of 40−50 mA and a voltage of 19 V. The fracture

morphologies were observed by SEM (FEI Quant 250).

3 Results

3.1 Starting materials

Figure 1 shows the OM images of annealed samples after rolling. The microstructures are presented in the RD−ND section. When the sample was annealed at 550 °C for 30 min (Fig. 1(a)), most of the grains were recrystallized with small grain size, and at the same time, several deformed grains remained. It can be observed from Figs. 1(b−d) that other annealed samples exhibited a homogeneous microstructure with equiaxed recrystallized grains. The fine grains were obviously grown up and the grain boundaries (GBs) became clearer as the annealing temperature and/or processing time increased. The average grain sizes of all annealed samples were measured by Nano Measure software and the corresponding grain size distributions are presented in Figs. 1(a−d). Under different annealing conditions, the average grain sizes of these samples were calculated to be 2, 9, 23, and 51 μm, which are labeled as D2, D9, D23, and D51 in the following discussion, respectively.

Figure 2 shows the EBSD orientation maps in
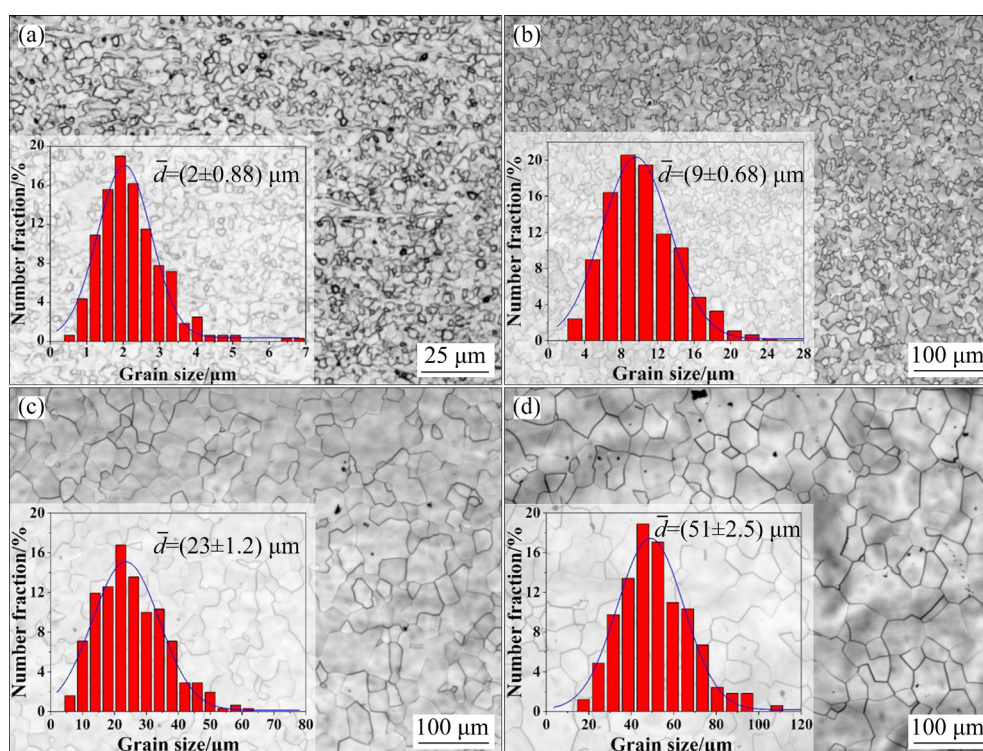
Fig. 1 OM images of starting materials with different annealing processes: (a) 550 °C, 30 min; (b) 650 °C, 30 min; (c) 750 °C, 30 min; (d) 750 °C, 60 min (The grain size distributions are presented in corresponding OM images)
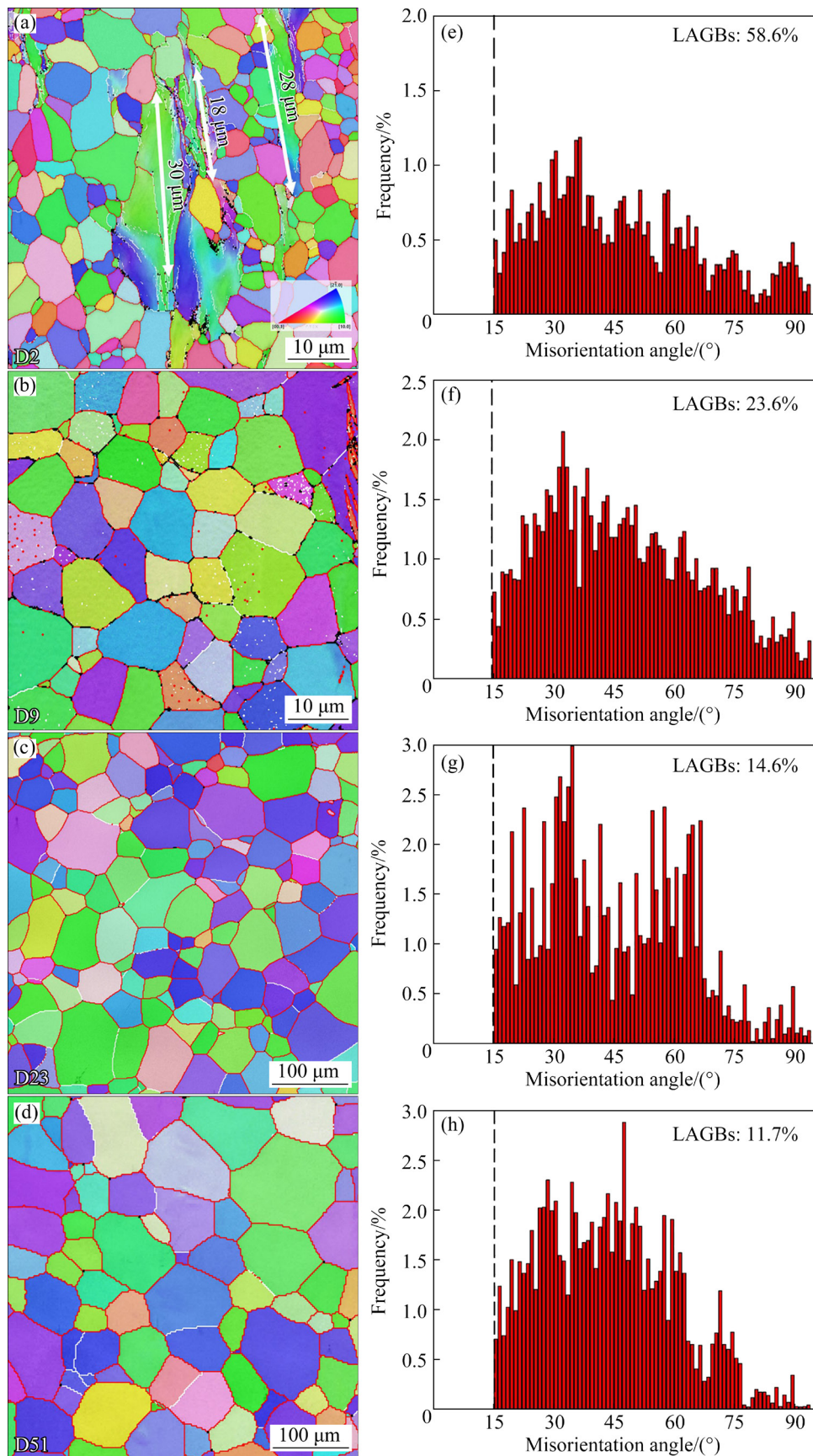
Fig. 2 EBSD maps of annealed samples (a−d) and corresponding misorientation angle distribution (e−h): (a, e) 550 °C, 30 min; (b, f) 650 °C, 30 min; (c, g) 750 °C, 30 min; (d, h) 750 °C, 60 min

inverse pole figure (IPF) form in the RD−ND section, where the RD direction was projected, as well as the corresponding misorientation distributions. The EBSD data were analyzed using the ATEX software [30]. The low-angle grain boundaries (LAGBs; $2°\leq\theta\leq15°$) and the high-angle grain boundaries (HAGBs; $\theta>15°$) were labeled by white and red lines, respectively. 5° was considered as a minimum disorientation angle for defining a grain. Some notable elongated grains with a length of more than 18 μm could be found in the D2 alloy (Fig. 2(a)), which indicated that the recrystallization was not completed under this heat treatment condition. As shown in Figs. 2(e−h), frequencies of LAGBs for D2, D9, D23, and D51 samples were 58.6%, 23.6%, 14.6%, and 11.7%, respectively, which revealed that the fraction of LAGBs was decreased by increasing the annealing temperature and/or time.

3.2 Tensile properties

Engineering strain−stress curves of tensile tests with various grain sizes are plotted in Fig. 3 and tensile properties are summarized in Table 1. Mechanical properties are distinct for samples with different grain sizes and/or under different processing temperatures. For the RT tested samples in Fig. 3(a), the D2 sample exhibited the best comprehensive mechanical properties where the yield strength (σ_y) was 481.7 MPa, the ultimate tensile strength (σ_b) was 529.8 MPa and the elongation to failure (EL) was 27.1%. It is notable that a clear yield plateau phenomenon of yield point elongation [31−34] at RT could be seen in the D2 sample, which was not found at LNT (Fig. 3(b)). This phenomenon only exists within a specific range of the average grain size (1−2 μm) for CP-Ti [33,34], which is induced by numerous dislocation multiplication locations in fine-grained structured samples [38] and is considered as a remarkable contribution in EL in RT tensile test. The EL of the D9 sample was slightly higher than that of the D2 sample. This phenomenon is possible to happen due to the heterogeneous microstructure in the D2 sample and possible twinning activation in the D9 sample. The EL of D23 and D51 samples decreased with the larger grain size. A similar result was reported in Ref. [35], where the EL of the sample with the grain size of 7.5 μm was smaller than that of the sample with grain size of 15.5 μm.
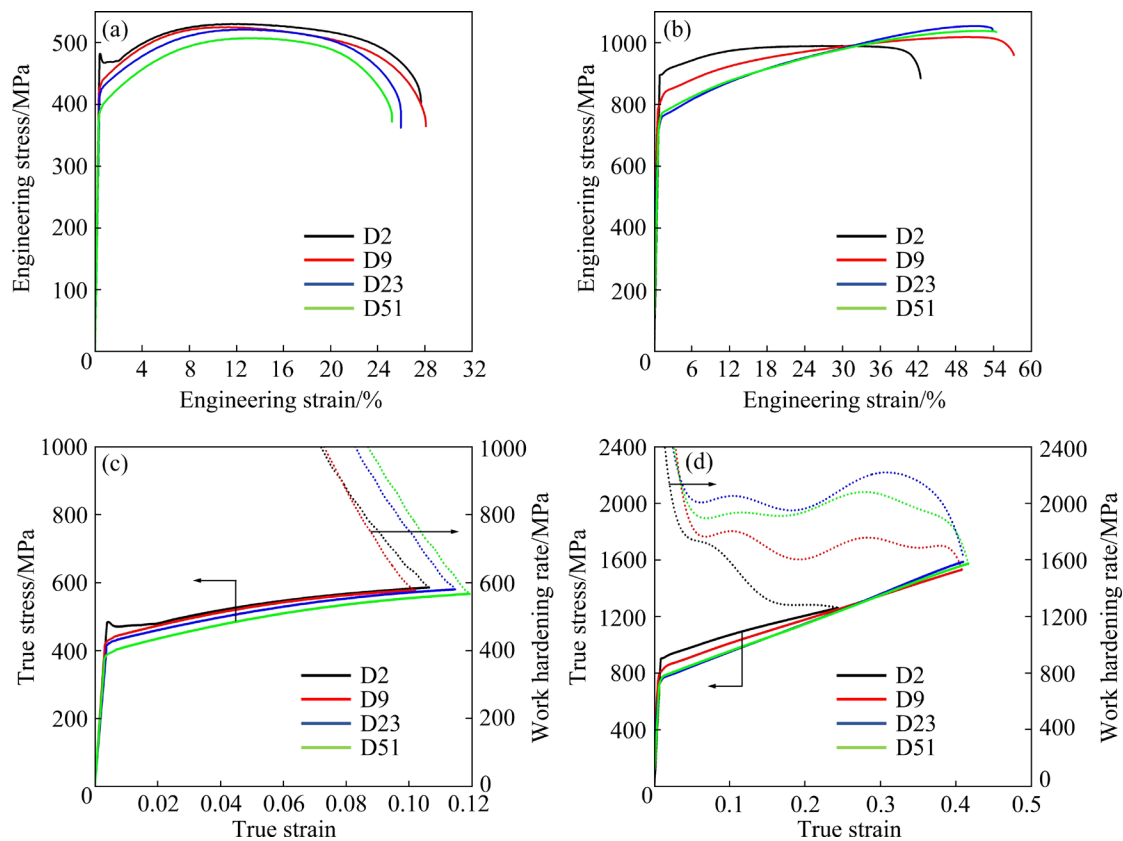
Fig. 3 Engineering strain−stress curves at RT (a) and LNT (b); True strain−stress curves and corresponding work hardening curves at RT (c) and LNT (d)

Table 1 Mechanical properties of samples with different grain sizes when tested at RT and LNT

Condition	Sample	σ_y/MPa	σ_b/MPa	EL/%	$d^{-1/2}$/μm$^{-1/2}$	$\Delta\sigma$/MPa
RT	D2	481.7±2.8	529.8±3.2	27.1±2.5	0.71	48
	D9	437.5±4.7	524.9±1.8	27.4±2.2	0.33	87
	D23	429.2±5.2	520.9±7.5	25.2±3.7	0.21	92
	D51	398.4±6.2	506.8±7.4	24.6±1.2	0.14	108
LNT	D2	896.2±9.8	988.5±8.7	41.4±4.5	0.71	92
	D9	796.6±6.8	1017.9±7.2	56.5±3.9	0.33	221
	D23	719.2±8.5	1053.2±9.7	53.2±4.3	0.21	334
	D51	721.4±6.1	1038.1±7.6	53.8±2.8	0.14	317

However, the grain size had no remarkable effect on the uniform elongation (UEL) at RT, showing about 12% for all the samples (Fig. 3(a)).

As shown in Fig. 3(b), all samples presented an excellent combination of strength and EL. Both strength and EL were almost twice higher when compared to that of the RT tested samples. The D2 alloy presented the highest σ_y of 896.2 MPa due to the smallest average grain size, whereas the D23 showed the highest σ_b of 1053.2 MPa with the lowest σ_y among all samples under the same condition. The stress increment ($\Delta\sigma=\sigma_b-\sigma_y$) was sharply increased at LNT compared with RT, especially for D23 and D51 alloy. Simultaneously, the UEL for the D9, D23, and D51 was more significantly increased than D2 as the gap between EL and UEL decreased from around 14% to 5% (Fig. 3(b)). Moreover, the true strain−stress and the corresponding work hardening curves before necking are illustrated in Figs. 3(c) and 3(d), respectively. It can be clearly seen that the work hardening rate at LNT was enhanced. The RT-tested samples showed the continuously decreasing work hardening rate where the deformation occurred homogeneously. However, the curves showed a falling−increasing−falling changing tendency with several peak values at LNT, and similar results were obtained in Ref. [36]. It was indicated that the deformation mechanism was possibly changed from RT to LNT.

3.3 Fracture morphologies

Figure 4 shows the SEM morphologies of the fracture surface of tensile-tested samples with different grain sizes and processing temperatures. Apparently, an amount of dimples could be observed in both RT-tested and LNT-tested samples,

which indicated the characteristics of ductile fracture [37]. The average sizes of dimples were measured by the software Nano measure, where the average dimple sizes at RT were 10.5, 28.3, 39.7 and 50.6 μm corresponding to D2, D9, D23 and D51, respectively. The dimple sizes of LNT-tested samples were 3.4, 6.6, 4.8 and 2.5 μm. It was abnormal that the D51 sample showed the smallest average dimple size. The results revealed that the grain size had an opposite impact on the dimple size at RT and LNT, which should be related to the difference in the deformation mechanism. When the tensile test was carried out at LNT, the generation of a large number of twins led to grain breakage in materials with relatively small grain sizes, which was the main reason for this phenomenon. In addition, the fracture morphology confirmed the EL results in Fig. 3, indicating that ductility could be improved by grain refinement [38].

3.4 Microstructure evolution

Microstructure evolution of tensile tested D2, D9 and D23 samples were further investigated to clarify the deformation behavior at RT and LNT. The microstructures absolutely varied from RT to LNT, which was closely related to the original grain size. After the samples were processed by tensile test at RT, the microstructures remained almost unchanged compared to the initial samples in Fig. 5. The results revealed that few deformation twins (DTs) with the small thicknesses could be found to form in some large grains of D2, D9 and D23 samples. In addition, the color gradients appeared within multiple grains in Figs. 5(a−c) and the numerous LAGBs were formed during the deformation process due to strain accumulation in the elongated grains. Therefore, the misorientation
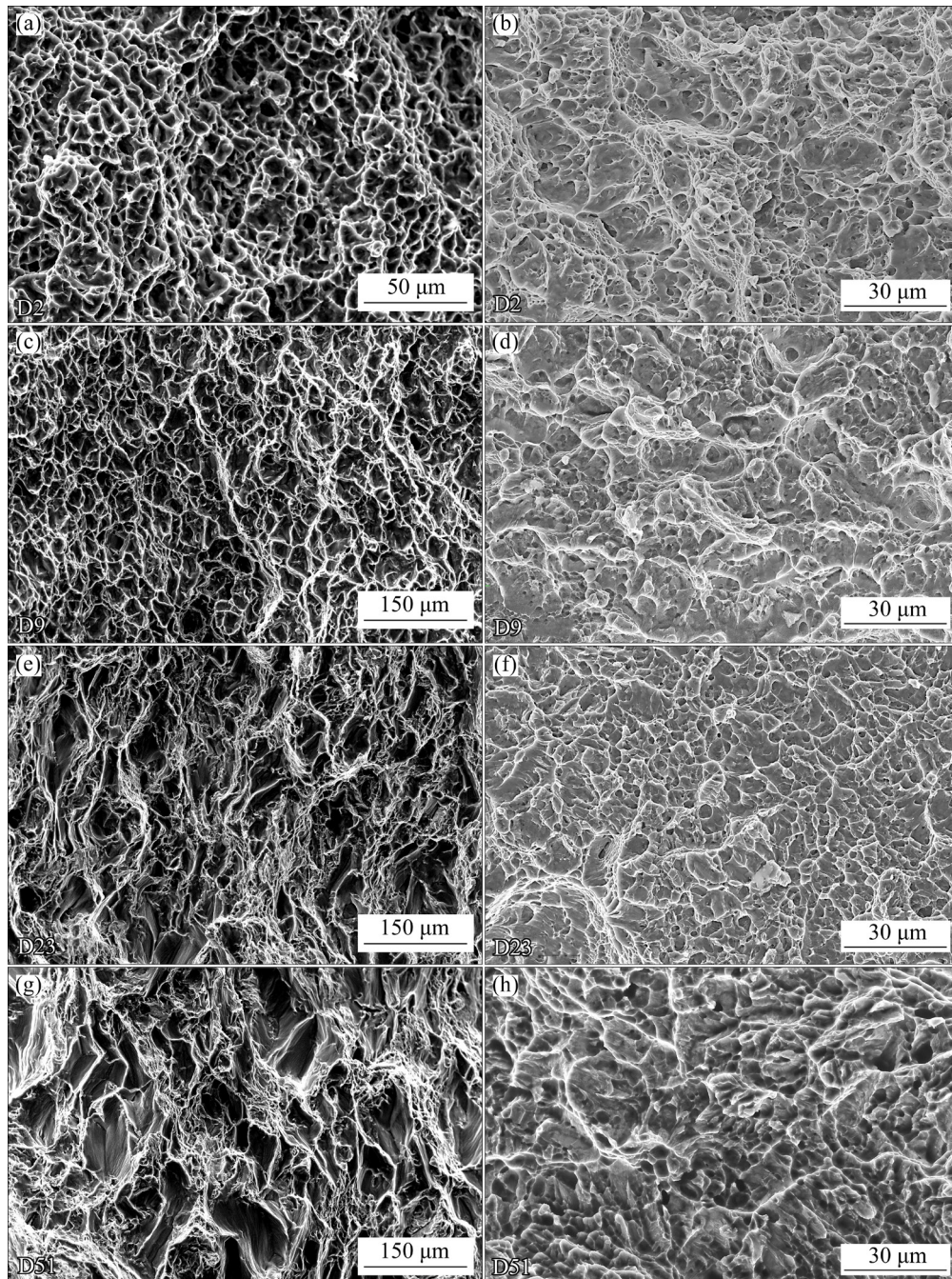
Fig. 4 Fracture surface morphologies by SEM: (a, c, e, g) RT-tested samples; (b, d, f, h) LNT-tested samples

distributions of RT-tested samples (Fig. 6(a)) were obviously changed compared to the initial samples (Figs. 2(e−h)). A distinctive misorientation peak around 85° newly appeared in the RT-tested samples, especially for D23, as shown in Fig. 6(a), which were induced by $\{10\bar{1}2\}\langle10\bar{1}1\rangle$ extension twins (ETs) [16,39]. The situations in the LNT-tested samples were different, where a higher density of DTs could be clearly observed compared with RT-tested samples. Especially for D9 and D23,

the coarse recrystallized grains were fragmented by the high density of DTs, which would further impact the texture. Figure 6(b) shows the misorientation distribution maps of LNT-tested samples. The new peaks around 65°, 85° and 48° were generated, which were related to $\{11\bar{2}2\}$-$\langle10\bar{2}3\rangle$ compression twins (CTs), $\{10\bar{1}2\}$ ETs and $\{11\bar{2}2\}$−$\{10\bar{1}2\}\langle\bar{5}50\bar{3}\rangle$ secondary twins, respectively [40,41]. It could be seen in Fig. 6(c) that the frequency of LAGBs was lower in the
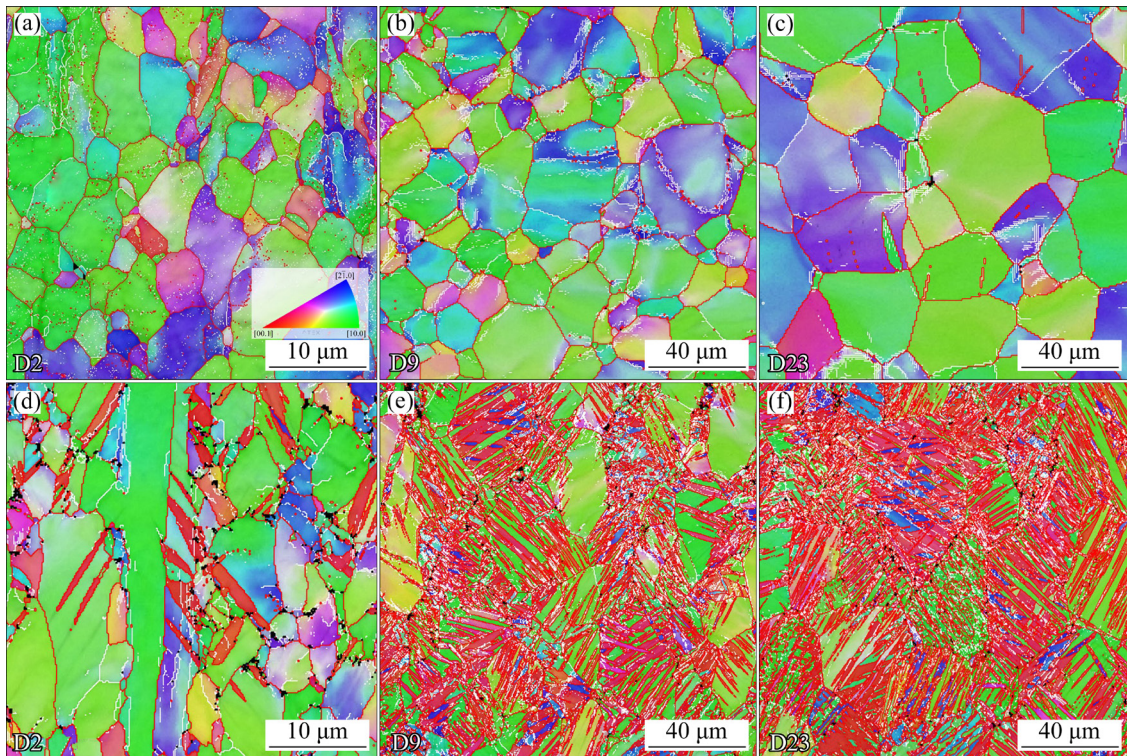
Fig. 5 Microstructure evolution of samples tested by EBSD: (a, b, c) At RT; (d, e, f) At LNT (The white lines and red lines represent the LAGBs and HAGBs, respectively)
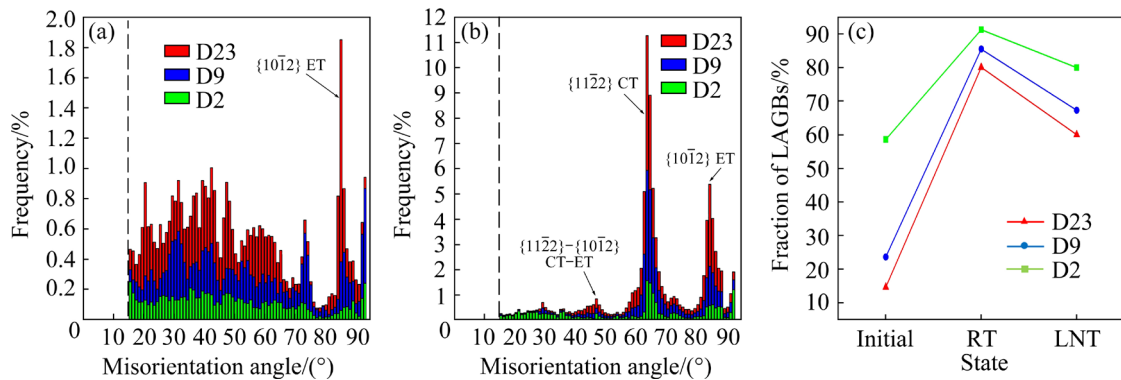
Fig. 6 Misorientation angle distribution of samples with different processes: (a) At RT; (b) At LNT; (c) Statistics of LAGBs in three processing states

initial condition, but dramatically increased after elongation at RT due to the formation of vast LAGBs inside the grains (Figs. 5(a−c)). When the samples were tested at LNT, a large number of twins introduced more HAGBs compared to those under RT, so the frequency of LAGBs was relatively lower.

3.5 Texture evolution

EBSD based texture evolution of D2, D9 and D23 samples in different processing conditions are presented by {0002} pole figures, as shown in

Fig. 7. As the recrystallization could not change the typical texture of rolled Ti alloy during the annealing process [13], the texture of annealed samples maintained the c-axis tilting from ND towards TD, as shown in Figs. 7(a, d, g). After being tested at RT and LNT, the texture component of the D2 alloy remained unchanged where the intensities of texture were enhanced from an initial 11.26 to 14.05 in the RT sample and 12.3 in the LNT sample, respectively. For D9 alloy, as shown in Figs. 7(d−f), the texture intensities of deformed samples decreased with compared to the initial one.
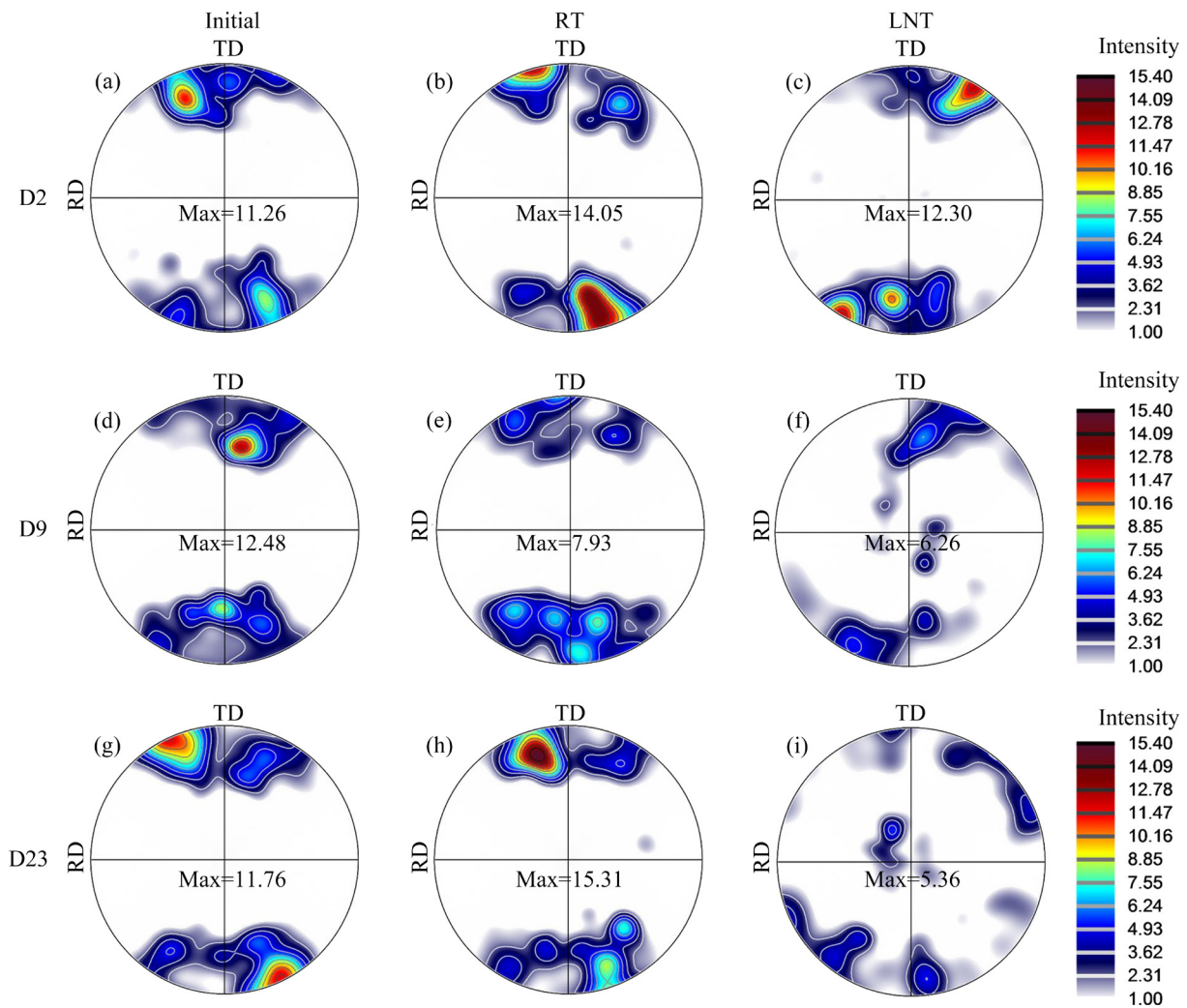
Fig. 7 EBSD based texture evolution by {0002} pole figure

It could be seen in Fig. 7(e) that the texture components were obviously changed with more discrete peak values, due to the change of internal grain misorientation. With the activation of vast twin variants, D9 (Fig. 7(f)) and D23 (Fig. 7(i)) showed nearly random texture with low intensity. Furthermore, an abnormal texture component of the *c*-axis nearly parallel to ND also appeared in Figs. 7(f, i), where the intensities were 3.75 and 5.36, respectively. The same results have been reported in cryogenic rolled CP-Ti sheets [42]. This abnormal texture was considered to be mainly related to $\{11\bar{2}2\}$ and $\{11\bar{2}4\}$ CTs.

4 Discussion

4.1 Deformation mechanism

In the HCP materials such as *α*-Ti alloy, it is well known that dislocation slip and twinning are the dominant deformation mechanisms. The activation of the deformation mode is strongly depended on the critical resolved shear stress (CRSS), which has strong temperature sensitivity. After tension at RT, deformation twinning was rarely observed in D2, D9 and D23 samples, and the plastic deformation was dominated by dislocation slip, as shown in Fig. 5 and Fig. 8. The DTs in RT-tested samples were confirmed to be the $\{10\bar{1}2\}$ ETs. These twin variants were more frequently generated in coarse grains, which have lower CRSS at RT with compared to other twin variants [43]. Simultaneously, the parallel slip bands [14] could be clearly seen in D2 and D9 samples compared with D23. The critical twinning stress of Ti was much lower than the CRSS for dislocation slip at LNT [5,12,44], so deformation mechanism was changed. A much higher density of DTs was activated at LNT (Figs. 8(d−f)), and new
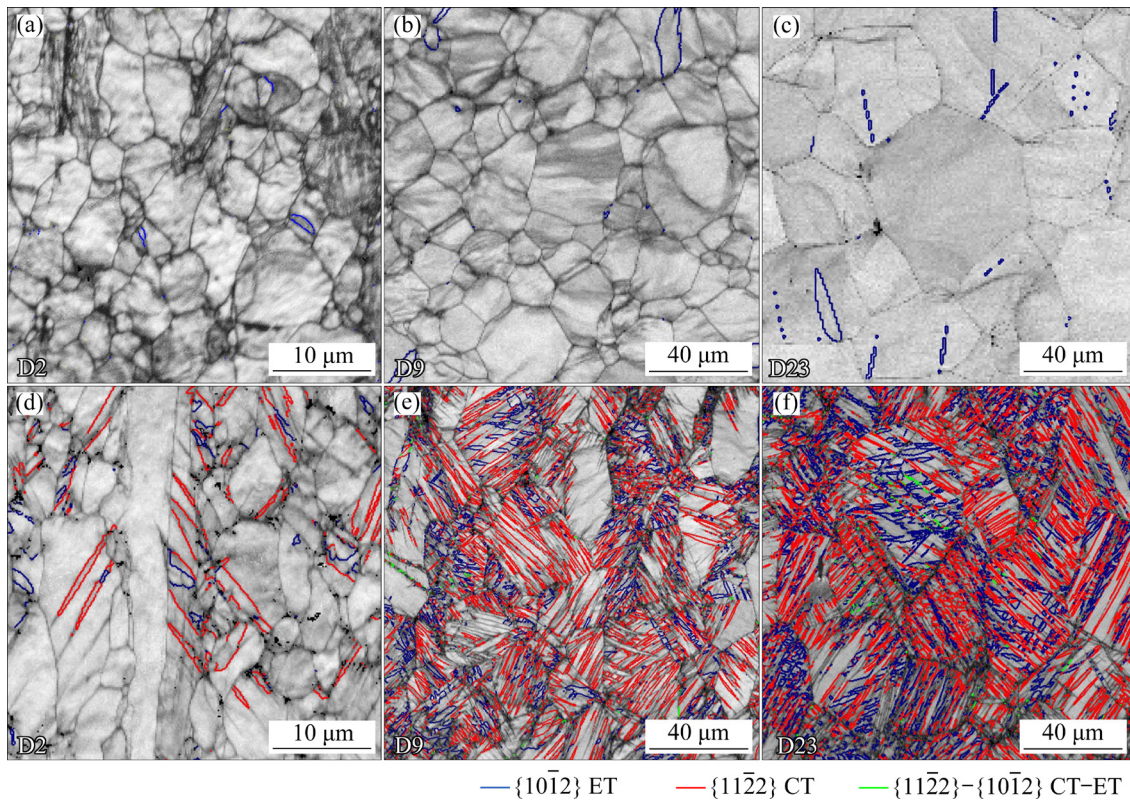
Fig. 8 Twinning observation of fractured samples at different processing temperature: (a, b, c) RT; (d, e, f) LNT

twin variants of $\{11\bar{2}2\}$ CTs and $\{11\bar{2}2\}-\{10\bar{1}2\}$ secondary twins were formed which were not observed in RD-tested samples. The matrixes were markedly fragmented, particularly in D9 and D23 samples. Moreover, in both RT- and LNT-tested samples, the density of DTs was strongly related to the grain size. It was shown in Fig. 9 that the length fraction of twins was higher in samples with larger grains. In D23 alloy, the length fraction of twins took up nearly 60% after being tested at LNT. Furthermore, the length fraction ratios of $\{10\bar{1}2\}$ ETs to $\{11\bar{2}2\}$ CTs at LNT were calculated to be 0.42, 0.49 and 0.75 for D2, D9 and D23. The relative proportion of $\{10\bar{1}2\}$ ETs was even higher in the material with larger grains, indicating that $\{11\bar{2}2\}$ CTs have higher sensitivity on grain size and deformation temperature [6]. The formation of this high density of twins leads to a significant increase in the work hardening rate [45] and benefits the improvement of mechanical properties, which can be confirmed by the tensile test results in Fig. 3.

Further discussion was based on the TEM observations which were performed near the fracture zone of all the samples, as shown in Figs. 10 and 11. Fractured samples showed various
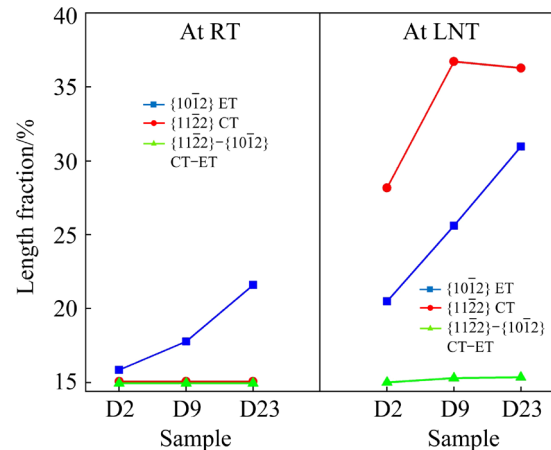
Fig. 9 Length fraction statistics of different twinning types in fractured samples

microstructure evolution in different grain sizes and processing temperatures. The high density of dislocation walls, dislocation tangles, and cells inside some deformed grains could be observed in D2 (Fig. 10(a)) and D9 (Fig. 10(b)) samples [46]. These features were generated in the vicinity of GBs. Nevertheless, the dislocation density was reduced in D23, and a number of dislocation lines could still be clearly observed in Fig. 10(c). More twins could be observed in D51 sample (Fig. 10(d))
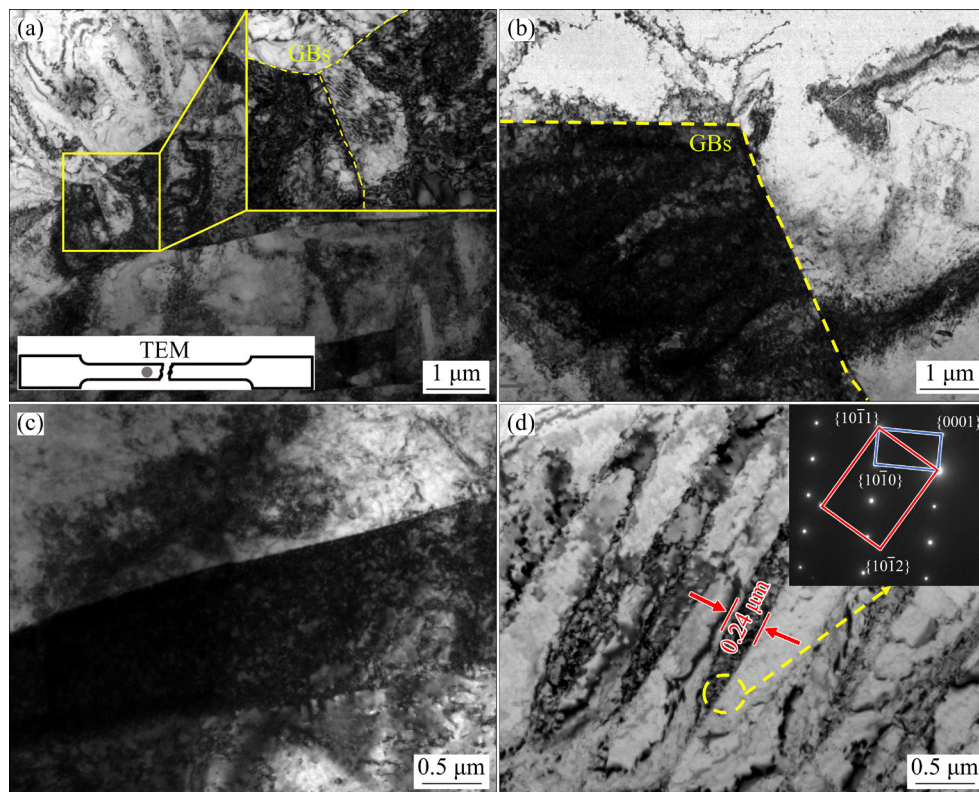
Fig. 10 TEM images close to fracture zone of RT-tested samples: (a) D2 sample; (b) D9 sample; (c) D23 sample; (d) D51 sample and related diffraction patterns (The yellow dotted lines indicate the GBs and twin thickness are highlighted by red marks)
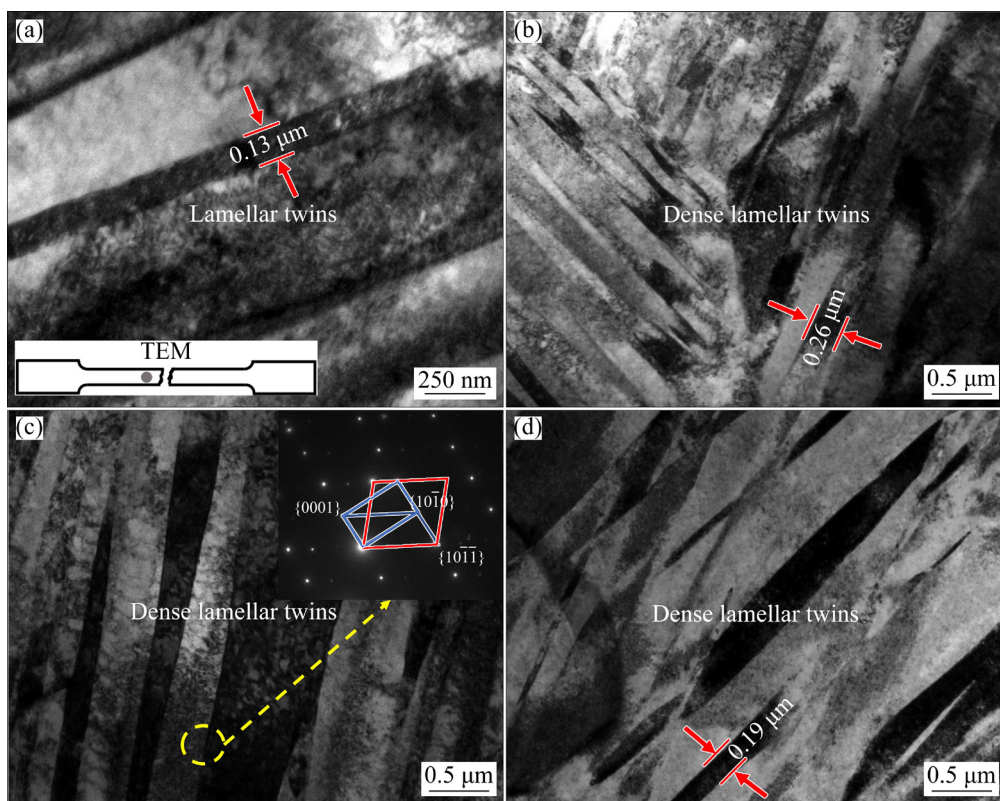
Fig. 11 TEM images close to fracture zone of LNT-tested samples: (a) D2 sample; (b) D9 sample; (c) D23 samples and related diffraction patterns; (d) D51 sample

while dislocation gathered within the DTs. The EBSD (Fig. 8) and TEM (Fig. 10) results demonstrated that the dislocation slip was the main deformation mechanism when tested at RT, especially in the D2 and D9 samples. DTs in D23 and D51 samples were more found due to the increased grain size. However, the proportion of those DTs was still low so that DTs could induce a limited effect on the mechanical properties.

On the contrary, the density of dislocations and mean dislocation motion free path reduced sharply at LNT as the DTs were gradually formed [44]. For the D2 sample, Fig. 11(a) showed that dislocation slip was still the main deformation mechanism while several DTs were formed with a thickness of about 0.13 μm. The YS of the D2 sample was the highest (Fig. 3(b)) at LNT due to the smallest average grain size; however, the other samples showed higher UTS and EL. The results indicated that the mechanical properties were related to not only the grain size but also the deformation mechanism at different processing temperatures. The abundant twin variants were activated to accommodate the imposed strain in D9, D23 and D51 samples, as shown in Figs. 11(b−d), and dense lamellar twins could be observed compared with the RT-tested samples. Generally, grain refinement induced by the twinning and lower density of dislocation collaborated to have an impact on the

work hardening of Ti alloy during tensile test [13], and twin boundaries would act as obstacles to the dislocation motion and conduct the matrix reorientations to benefit the dislocation slip [20]. Thus, the UTS of the D9, D23 and D51 samples at LNT (Fig. 3(b)) was much improved and even higher than that of the D2 sample. Twinning induced plasticity [47] was considered to interpret the appeared outstanding ductility in LNT-tested samples [48]. The thickness of several DTs was measured in Figs. 10 and 11, and the results revealed that the twins were relatively thin in the LNT-tested samples. Moreover, the reorientation mechanism of the matrix for the benefit of dislocation slip caused by twinning and the interaction of boundary interfaces are worthy to be further investigated.

4.2 Hall−Petch relationship

The well-known Hall−Petch relationship reveals that the grain refinement induces the improvement of YS (σ_y) in materials, which is commonly expressed by the following formula [6]:

$$\sigma_y = \sigma_0 + k_{HP} d^{-1/2} \tag{1}$$

where σ_0 is the stress of an infinite single crystal, k_{HP} is the Hall−Petch coefficient and d represents the average grain size.

As shown in Fig. 12(a), σ_y is almost linearly
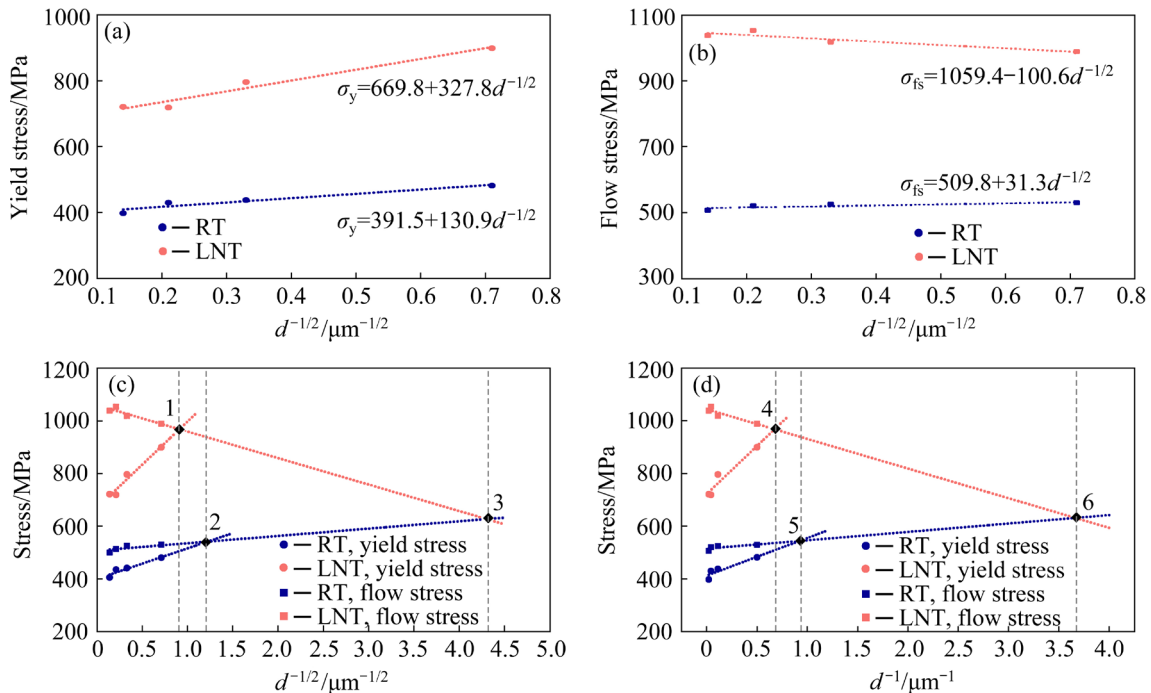
Fig. 12 Hall−Petch relationship of tensile tested samples for yield stress (a) and flow stress (b), and data plotted against $d^{-\chi}$ with χ=1/2 (c) and χ=1 (d)

Table 2 Fitting parameters of Hall−Petch relation at RT and LNT

Condition	Stress	$\chi=1/2$			$\chi=1$			$\chi=1/4$		
		σ_0/MPa	k/(MPa·μm$^{1/2}$)	R^2	σ_0/MPa	k/(MPa·μm)	R^2	σ_0/MPa	k/(MPa·μm$^{1/4}$)	R^2
RT	σ_y	391.5	130.9	0.92	419.4	135.8	0.78	343.6	166.0	0.95
	σ_{fs}	509.8	31.3	0.65	510.9	36.2	0.33	497.0	42.0	0.74
LNT	σ_y	669.8	327.8	0.96	722.4	363.9	0.98	554.4	407.7	0.96
	σ_{fs}	1059.4	−100.6	0.85	1043.4	−112.4	0.96	1094.3	−124.0	0.85

related to $d^{-1/2}$ at both RT and LNT, which agrees with the Hall−Petch relationship. As the fine grains provide more GBs, the dislocation motion and multiplication will be hindered and higher stress is needed to be imposed for plastic deformation. However, the deformation mechanism is quite different at LNT where the necking is delayed compared to RT. The flow stress (σ_{fs}) in necking shows a negative coefficient at LNT. Since only the grain boundary strengthening is considered in the conventional Hall−Petch formula, DUNSTAN and BUSHB [49] have proposed a modified Hall−Petch relationship that can well fit the cryogenic deformation with both grain boundary and twinning strengthening [20]:

$$\sigma_y=\sigma_0+k_{HP}d^{-\chi} \tag{2}$$

where exponent χ value is widely scattered from 0.2 to 1, as the Hall−Petch formula is included when $\chi=0.5$. In Table 2, different χ values of 1/4, 1/2 and 1 are chosen to fit the results presented in Figs. 12(b, d). The result shows the highest fitting regression R^2 when the χ value is taken as 1. Besides, the fitted lines of yield stress and flow stress are extended until intersected. The points of intersection 1, 2, 4 and 5 (Figs. 12(c, d)) indicate that σ_y is equal to σ_{fs} and will finally exceed it with decreasing the grain size. Moreover, it can also predict the possible limited grain size for twinning activation from Points 3 and 6, because it is difficult to generate twins in ultra-fine grains even at LNT. The better predicted grain size is 0.27 μm calculated by Point 6 with $\chi=1$. The modified Hall−Petch relationship provides a validated law for the study of the relationship between deformation mechanism and strength under cryogenic condition.

5 Conclusions

(1) The recrystallized CP-Ti samples with different grain sizes exhibited an excellent combination of high strength and EL when deformed at LNT compared to RT. The D2 sample had the highest YS at both RT and LNT due to the smallest grain size; however, the UTS and EL of D9, D23 and D51 samples at RT were much lower than those at LNT due to the transition of deformation mechanism. In addition, the UTS and EL of D9, D23 and D51 samples at LNT showed an inverse evolution compared to RT.

(2) Dislocation slip was the main deformation mode and only a few {10$\bar{1}$2} ETs could be observed for all samples at RT. However, deformation twinning became the dominant deformation mechanism at LNT. A high density of {10$\bar{1}$2} ETs and {11$\bar{2}$2} CTs and some {11$\bar{2}$2}−{10$\bar{1}$2} secondary twins were generated. The formation of various new orientations and the related grain refinement induced by the profuse twins contributed to the high performance and work hardening rate of samples at LNT.

(3) A modified Hall−Petch relationship was proposed for the strengthening mechanism of tensile tested CP-Ti sample under cryogenic deformation condition.

References

[1] BANERJEE D, WILLIAMS J C. Perspectives on titanium science and technology [J]. Acta Materialia, 2013, 61: 844−879.

[2] NASERI R, KADKHODAYAN M, SHARIATI M. Static mechanical properties and ductility of biomedical ultrafine-grained commercially pure titanium produced by ECAP process [J]. Transactions of Nonferrous Metals Society of China, 2017, 27: 1964−1975.

[3] YAN Shao-kun, SONG Guang-ling, LI Zheng-xian, WANG Hao-nan, ZHENG Da-jiang, CAO Fu-yong, HORYNOVA M, DARGUSCH M S, ZHOU Lian. A state-of-the-art review on passivation and biofouling of Ti and its alloys in marine environments [J]. Journal of Materials Science & Technology, 2018, 34: 421−435.

[4] WANG Q, REN J Q, ZHANG B B, XIN C, WU Y K, ZHANG L. Simultaneously improved strength and elongation at cryogenic temperature in Ti−5Al−1V−1Sn−1Zr−0.8Mo alloy with a bimodal structure [J]. Materials Science and Engineering A, 2021, 824: 141792.

[5] ZANG M C, NIU H Z, YU J S, ZHANG H R, ZHANG T B, ZHANG D L. Cryogenic tensile properties and deformation behavior of a fine-grained near alpha titanium alloy with an equiaxed microstructure [J]. Materials Science and Engineering A, 2022, 840: 142952.

[6] STANFORD N, CARLSON U, BARNETT M R. Deformation twinning and the Hall–Petch relation in commercial purity Ti [J]. Metallurgical and Materials Transactions A, 2008, 39: 934−944.

[7] WANG Qi, REN Jun-qiang, WANG Yin-ling, XIN Chao, XIAO Lin, YANG Dan. Deformation and fracture mechanisms of gradient nanograined pure Ti produced by a surface rolling treatment [J]. Materials Science and Engineering A, 2019, 754: 121−128.

[8] HE Yong-sheng, HU Rui, LUO Wen-zhong, HE Tao, LAI Yun-jin, DU Yu-jun, LIU Xiang-hong. Microstructural evolution and creep deformation behavior of novel Ti−22Al−25Nb−1Mo−1V−1Zr−0.2Si (at.%) orthorhombic alloy [J]. Transactions of Nonferrous Metals Society of China, 2019, 29: 313−321.

[9] YAN Wen-gao, WANG Hua-ming, TANG Hai-bo, CHENG Xu, ZHU Yan-yan. Effect of Nd addition on microstructure and tensile properties of laser additive manufactured TC11 titanium alloy [J]. Transactions of Nonferrous Metals Society of China, 2022, 32: 1501−1512.

[10] ALANKAR A, EISENLOHR P, RAABE D. A dislocation density-based crystal plasticity constitutive model for prismatic slip in α-titanium [J]. Acta Materialia, 2011, 59: 7003−7009.

[11] WRONSKI S, WIERZBANOWSKI K, JĘDRYCHOWSKI M, TARASIUK J, WRONSKI M, BACZMANSKI A, BACROIX B. Microstructure evolution of titanium after tensile test [J]. Materials Science and Engineering A, 2016, 656: 1−11.

[12] WANG L, ZHENG Z, PHUKAN H, KENESEI P, PARK J S, LIND J, SUTER R M, BIELER T R. Direct measurement of critical resolved shear stress of prismatic and basal slip in polycrystalline Ti using high energy X-ray diffraction microscopy [J]. Acta Materialia, 2017, 132: 598−610.

[13] WRONSKI S, JEDRYCHOWSKI M, TARASIUK J, BACROIX B. Microstructure evolution of titanium after tensile and recrystallisation [J]. Materials Science and Engineering A, 2017, 692: 113−126.

[14] XIN Chao, WANG Qi, REN Jun-qiang, ZHANG Yong-hong, WU Jin-ping, CHEN Jie, ZHANG Liang, SANG Biao, LI Le. Plastic deformation mechanism and slip transmission behavior of commercially pure Ti during in situ tensile deformation [J]. Metals, 2022, 12: 721.

[15] XU Shun, ZHOU Ping, LIU Gui-sen, XIAO Da-wu, GONG Ming-yu, WANG Jian. Shock-induced two types of $\{10\bar{1}2\}$ sequential twinning in Titanium [J]. Acta Materialia, 2019, 165: 547−560.

[16] ZHOU Bao-xue, YANG Rong, WANG Bing-shu, DENG Li-ping, ZHANG Yong-hao. Twinning behavior of pure titanium during rolling at room and cryogenic temperatures [J]. Materials Science and Engineering A, 2021, 803: 140458.

[17] WON J W, CHOI S W, HONG J K, SUH B C, LEE J H, KWAK B J. Microstructure and strength–ductility balance of pure titanium processed by cryogenic rolling at various rolling reductions [J]. Materials Science and Engineering A, 2020, 798: 140328.

[18] WON J W, LEE J H, JEONG J S, CHOI S W, LEE D J, HONG J K, HYUN Y T. High strength and ductility of pure titanium via twin-structure control using cryogenic deformation [J]. Scripta Materialia, 2020, 178: 94−98.

[19] CHOI S W, WON J W, LEE S, HONG J K, CHOI Y S. Deformation twinning activity and twin structure development of pure titanium at cryogenic temperature [J]. Materials Science and Engineering A, 2018, 738: 75−80.

[20] HUANG Zhao-wen, WEN Dong-hui, HOU Xiao-dong, LI Yu-sheng, WANG Biao, WANG An-ding. Grain size and temperature mediated twinning ability and strength−ductility correlation in pure titanium [J]. Materials Science and Engineering A, 2022, 849: 143461.

[21] ZHEREBTSOV S V, DYAKONOV G S, SALEM A A, SOKOLENKO V I, SALISHCHEV G A, SEMIATIN S L. Formation of nanostructures in commercial-purity titanium via cryorolling [J]. Acta Materialia, 2013, 61: 1167−1178.

[22] LUO Jin-rui, SONG Xiao, WANG Mao-yin. Effects of different types of twinning on microstructure and mechanical properties of a strongly textured TA2 commercially pure titanium alloy subjected to rolling at ambient and cryogenic temperatures [J]. Journal of Iron and Steel Research International, 2018, 25: 275−281.

[23] YU Hai-liang, WANG Lin, YAN Ming, GU Hao, ZHAO Xing, KONG C, WANG Yu, PESIN A, ZHILYAEV A P, LANGDON T G. Microstructural evolution and mechanical properties of ultrafine-grained Ti fabricated by cryorolling and subsequent annealing [J]. Advanced Engineering Materials, 2020, 22: 1901463.

[24] CHOI S W, JEONG J S, WON J W, HONG J K, CHOI Y S. Grade-4 commercially pure titanium with ultrahigh strength achieved by twinning-induced grain refinement through cryogenic deformation [J]. Journal of Materials Science & Technology, 2021, 66: 193−201.

[25] LEE S, CHOE H J, HYUN Y T, LEE D W, WON J W. In-plane tensile deformation and formability of pure titanium sheet at cryogenic temperature [J]. Materials Science and Engineering A, 2022, 853: 143777.

[26] YIN Yan-fei, XU Wei, SUN Qiao-yan, XIAO Lin, SUN Jun. Deformation and fracture behavior of commercially pure

titanium with gradient nano-to-micron-grained surface layer [J]. Transactions of Nonferrous Metals Society of China, 2015, 25: 738−747.

[27] YUMAK N, ASLANTAS K, PEKBEY Y. Effect of cryogenic and aging treatments on low-energy impact behaviour of Ti−6Al−4V alloy [J]. Transactions of Nonferrous Metals Society of China, 2017, 27: 514−526.

[28] WANG Bing-shu, LIU Hui-min, ZHANG Yong-gan, ZHOU Bao-xue, DENG Li-ping, WANG Chen, CHEN Jun-feng, ZHANG Yong-hao. Effect of grain size on twinning behavior of pure titanium at room temperature [J]. Materials Science and Engineering A, 2021, 827: 142060.

[29] KUMAR M A, BEYERLEIN I J. Influence of plastic properties on the grain size effect on twinning in Ti and Mg [J]. Materials Science and Engineering A, 2020, 771: 138644.

[30] BEAUSIR B, FUNDENBERGER J J. Analysis tools for electron and X-ray diffraction, ATEX-software [EB/OL]. www.atex- software.eu, Université de Lorraine - Metz, 2017.

[31] LUO Xuan, FENG Zong-qiang, YU Tian-bo, LUO Jun-qian, HUANG Tian-lin, WU Gui-lin, HANSEN N, HUANG Xiao-xu. Transitions in mechanical behavior and in deformation mechanisms enhance the strength and ductility of Mg−3Gd [J]. Acta Materialia, 2020, 183: 398−407.

[32] LI R G, SONG P F, WU G L, LIU B S, PAN H C, LI J R, ZHANG H. Tensile yielding plateau in fine-grained Mg−15Gd binary alloy [J]. Materials Letters, 2022, 324: 132757.

[33] LI Zhi-ming, FU Li-ming, FU Bin, SHAN Ai-dang. Yield point elongation in fine-grained titanium [J]. Materials Letters, 2013, 96: 1−4.

[34] SHI Xiao-hui, CAO Zu-han, FAN Zhi-yuan, GUO Rui-peng, QIAO Jun-wei. Probing into the yield plateau phenomenon in commercially pure titanium during tensile tests [J]. Acta Metallurgica Sinica (English Letters), 2020, 34: 701−709.

[35] ZHU Cheng-xi, XU Jie, YU Hai-ping, SHAN De-bin, GUO Bin. Size effect on the high strain rate micro/meso-tensile behaviors of pure titanium foil [J]. Journal of Materials Research and Technology, 2021, 11: 2146−2159.

[36] SHI Xiao-hui, FAN Zhi-yuan, CAO Zu-han, GUO Rui-peng, QIAO Jun-wei. Quasi-static tensile behaviors, mechanisms, and constitutive descriptions of commercially pure titanium at diverse strain rates in ambient air and liquid nitrogen [J]. Journal of Materials Engineering and Performance, 2021, 30: 944−954.

[37] ZHANG Hao, LI Xun-peng, GAO Tao, SONG Hai-peng, HUANG Gan-yuan. Experimental study on deformation evolution and fracture behaviors of pure titanium at different stress triaxialities [J]. Engineering Fracture Mechanics, 2021, 258: 108127.

[38] XIAO J F, SHANG X K, LI Y, GUAN Q W, HE B. Grain size-dependent tensile behaviour in a metastable beta titanium alloy [J]. Materials Science and Technology, 2022, 38: 469−483.

[39] TIRRY W, NIXON M, CAZACU O, COGHE F, RABET L. The importance of secondary and ternary twinning in compressed Ti [J]. Scripta Materialia, 2011, 64: 840−843.

[40] XU Shun, TOTH L S, SCHUMAN C, LECOMTE J S, BARNETT M R. Dislocation mediated variant selection for secondary twinning in compression of pure titanium [J]. Acta Materialia, 2017, 124: 59−70.

[41] XU Shun, GONG Ming-yu, JIANG Yan-yao, SCHUMAN C, LECOMTE J S, WANG Jian. Secondary twin variant selection in four types of double twins in titanium [J]. Acta Materialia, 2018, 152: 58−76.

[42] SONG Xiao, LUO Jin-ru, ZHANG Ji-shan, ZHUANG Lin-zhong, CUI Hua, QIAO Yi. Twinning behavior of commercial-purity titanium subjected to cryorolling [J]. The Journal of the Minerals, Metals & Materials Society, 2019, 71: 4071−4078.

[43] MA Zhi-cao, TANG Xiao-zhi, MAO Yong, GUO Ya-fang. The plastic deformation mechanisms of hcp single crystals with different orientations: Molecular dynamics simulations [J]. Materials, 2021, 14: 733.

[44] ZANG M C, NIU H Z, ZHANG H R, TAN H, ZHANG D L. Cryogenic tensile properties and deformation behavior of a superhigh strength metastable beta titanium alloy Ti−15Mo−2Al [J]. Materials Science and Engineering A, 2021, 817: 141344.

[45] BECKER H, PANTLEON W. Work-hardening stages and deformation mechanism maps during tensile deformation of commercially pure titanium [J]. Computational Materials Science, 2013, 76: 52−59.

[46] LU H F, LUO K Y, WU L J, CUI C Y, LU J Z. Effects of service temperature on tensile properties and microstructural evolution of CP titanium subjected to laser shock peening [J]. Journal of Alloys and Compounds, 2019, 770: 732−741.

[47] COOMAN D B C, ESTRIN Y, KIM S K. Twinning-induced plasticity (TWIP) steels [J]. Acta Materialia, 2018, 142: 283−362.

[48] FU Yu, XIAO Wen-long, KENT D, DARGUSCH M S, WANG Jun-shuai, ZHAO Xin-qing, MA Chao-li. Ultrahigh strain hardening in a transformation-induced plasticity and twinning-induced plasticity titanium alloy [J]. Scripta Materialia, 2020, 187: 285−290.

[49] DUNSTAN D J, BUSHBY A J. Grain size dependence of the strength of metals: The Hall−Petch effect does not scale as the inverse square root of grain size [J]. International Journal of Plasticity, 2014, 53: 56−65.

晶粒尺寸和温度对工业纯钛变形机制的影响

陈　才 [1]，韩冬生 [1]，宋玉涛 [2]，王名川 [1]，李玉胜 [2]，徐　舞 [3]，杨　森 [4]，刘吉梓 [2,5]

1. 南京理工大学 中法工程师学院，南京 210094；
2. 南京理工大学 材料科学与工程学院 纳米异构材料中心，南京 210094；
3. 北京理工大学 材料科学与工程学院 冲击环境材料技术国家级重点实验室，北京 100081；
4. 南京理工大学 材料科学与工程学院，南京 210094；
5. 南京理工大学 分析测试中心，南京 210094

摘　要：为了研究晶粒尺寸和加工温度对工业纯钛变形行为的影响，分别在室温和液氮温度下对平均晶粒尺寸为 2、9、23 和 51 μm 的样品进行单轴拉伸实验，采用背散射电子衍射技术(EBSD)和透射电子显微镜技术(TEM)表征样品的显微组织和织构。结果表明，室温条件下位错滑移是主要的变形机制，而液氮温度下拉伸的样品中有丰富的变形孪晶被激活，其中包括{10$\bar{1}$2}拉伸孪晶、{11$\bar{2}$2}压缩孪晶和{11$\bar{2}$2}−{10$\bar{1}$2}二次孪晶。这揭示液氮温度条件下塑性变形模式从位错滑移到动态孪生的转变，这也是具有较大晶粒尺寸的样品在液氮温度下依然具有优异力学性能的主要原因。另外，还提出了一种改进的 Hall−Petch 关系式，可用于在液氮温度条件下定量表征平均晶粒尺寸和孪晶对工业纯钛拉伸屈服强度的影响。

关键词：工业纯钛；低温拉伸试验；变形孪生；晶粒尺寸；晶体学织构

(Edited by Bing YANG)